

PAPER

[View Article Online](#)
[View Journal](#) | [View Issue](#)Cite this: *J. Mater. Chem. A*, 2026, **14**, 11057Cathode properties of MgV_2O_4 spinel for magnesium rechargeable batteries: effect of synthesis route on structure and electrochemical performanceNaoya Ishida,^{ID}*^a Keigo Kubota,^{ID}^a Toshikatsu Kojima,^{ID}^a Toshihiko Mandai,^{ID}^b Shin Kiyohara,^{ID}^c Yu Kumagai,^{ID}^c and Tetsu Ichitsubo,^{ID}^c

Magnesium rechargeable batteries (MRBs) are promising candidates for next-generation energy storage owing to their high volumetric capacity and safety. Herein, we investigate spinel-type MgV_2O_4 (MVO) as a cathode material and elucidate the correlation between its crystal structure and electrochemical performance. An ordered spinel was synthesized via a solid-state route and subsequently subjected to mechanical milling (MM), while a solvothermal (ST) method was employed to prepare a comparative sample. Rietveld refinement revealed that MM induces a transition from an ordered to a disordered spinel structure, accompanied by partial V occupancy at the interstitial 16c site, which obstructs Mg^{2+} migration between 8a sites. Despite particle size reduction, MM-MVO exhibited poor reversibility due to this structural disorder. Complementary computational analysis confirmed the energetic favorability of V migration into the 16c site by MM, explaining the origin of the diffusion barrier. In contrast, ST-MVO retained a relatively ordered structure with minimal V occupation at 16c sites and delivered a reversible capacity of 175 mAh g^{-1} at 2 V when paired with a high-voltage electrolyte. These findings highlight the critical role of spinel ordering in enabling efficient Mg^{2+} transport and provide design guidelines for high-performance MRB cathodes.

Received 25th November 2025
Accepted 6th February 2026

DOI: 10.1039/d5ta09602b

rsc.li/materials-a

1 Introduction

Lithium-ion batteries (LIBs) have dominated the field of rechargeable energy storage owing to their high energy density and excellent cycling stability. However, the limited availability and uneven geographical distribution of lithium resources have raised concerns regarding the long-term sustainability and cost of LIB technology. Consequently, the development of next-generation rechargeable batteries that do not rely on lithium has become an important global research focus.¹ Among various alternatives, the magnesium rechargeable battery (MRB) is a particularly attractive candidate. The first prototype MRB was reported by Aurbach *et al.* in 2000, demonstrating the feasibility of reversible magnesium deposition and dissolution.² Magnesium offers several intrinsic advantages: (i) as a divalent ion, Mg^{2+} can transfer two electrons per ion, enabling a higher

theoretical capacity than monovalent Li^+ ; (ii) its ionic radius (0.72 \AA) in six coordination is comparable to that of Li^+ (0.76 \AA),³ suggesting that magnesium-based cathodes could potentially achieve twice the specific capacity in LIBs. On the other hand, the strong coulombic interaction between Mg^{2+} ions and the host lattice often leads to sluggish diffusion kinetics, which remains a key challenge.⁴ Metallic magnesium itself possesses a high volumetric capacity of 3833 mAh cm^{-3} , approximately twice that of lithium metal (2061 mAh cm^{-3}). Furthermore, its high melting point ($\sim 650^\circ\text{C}$) ensures thermal stability under high-temperature operation,^{5,6} and its dendrite-less deposition behavior offers significant safety advantages.⁷ Thus, temperature-assisted operation may mitigate the sluggish Mg^{2+} ion diffusion to some extent.

The cell constructed of chevre-phase cathodes with magnesium metal anodes and grignard-based electrolytes has demonstrated excellent cyclability, exceeding 2000 cycles, reflecting the intrinsic durability of the MRB system.^{2,8} Nevertheless, such systems generally exhibit low operating voltages and limited capacities, emphasizing the need for improved cathode materials and more oxidative-stable electrolytes. Recent progress has achieved enhanced cycling performance, yet further capacity improvement remains a major objective. In this context, oxide-based cathodes, *e.g.* MgCo_2O_4 (ref. 9,10) and

^aResearch Institute of Electrochemical Energy, National Institute of Advanced Industrial Sciences and Technology (AIST), 1-8-31 Midorigaoka, Ikeda, Osaka 563-8577, Japan. E-mail: naoya-ishida@aist.go.jp

^bFunctional Electrolyte Synthesis Team, Research Center for Energy and Environmental Materials (GREEN), National Institute for Materials Science (NIMS), 1-1 Namiki, Tsukuba, Ibaraki, 305-0044, Japan

^cInstitute for Materials Research (IMR), Tohoku University, 2-1-1 Katahira, Aoba-ku, Sendai, 980-8577, Japan



delithiated $\text{Li}_2\text{FeSiO}_4$ (ref. 11) are of particular interest due to their superior air stability and high capacities compared to sulfide-based materials. Our previous studies in delithiated layered cathode-materials^{12,13} have shown that oxide-type cathodes can achieve the highest capacities (greater than 400 mAh g^{-1}) among reported oxide cathodes of MRB,¹⁴ demonstrating the theoretical potential for twice the capacity of LIBs, albeit with remaining cycling limitations. The use of an ionic liquid-based electrolyte incorporating the fully-solvated Mg complex, $[\text{Mg}(\text{G4})][\text{TFSA}]_2$ (TFSA: bis(trifluoromethanesulfonyl)amide), as a conductive salt, which exhibits a wide electrochemical stability window, is especially effective for extracting the intrinsic potential of oxide cathodes.^{15–17}

Spinel-type MgTM_2O_4 (TM = transition metal) have frequently been investigated as Li-free cathode materials, owing to their well-ordered 8a–16c–8a Mg^{2+} conduction pathways and structural robustness.^{9,10,18–22} Most reported spinel-type MgTM_2O_4 compounds operate as insertion-type (discharge-first) materials, while deintercalation-type (charge-first) spinels remain relatively unexplored. Among these, MgV_2O_4 (hereafter denoted as MVO) is a promising candidate because the $\text{V}^{3+/4+}$ redox couple may enable reversible Mg deintercalation at moderate voltages. In contrast, in vanadium spinels containing V^{4+} species (e.g., $\text{Mg}_4\text{V}_5\text{O}_{12}$ -type compounds²³), oxidation of V^{3+} is limited, suggesting that MVO without V^{4+} components is more suitable as a high-voltage cathode. Recently, solvothermally (ST) synthesized cactus-like MVO particles have shown excellent electrochemical performance, attributed to their shortened Mg^{2+} diffusion paths and abundant reactive surfaces.²⁴ However, due to the low oxidation resistance of the electrolyte, the electrochemical properties of ST-MVO have been evaluated in the region below 2 V, limiting the capacity to about 100 mAh g^{-1} (partial $\text{V}^{3+/2+}$ redox). If the characteristics are evaluated using an electrolyte with a higher potential, it becomes clear that the theoretical capacity of 282 mAh g^{-1} can be achieved by using $\text{V}^{3+/4+}$ redox. Moreover, solid-state synthesized MVO has scarcely been investigated. If a well-ordered normal spinel can be obtained *via* solid-state synthesis and subsequently refined into fine particles by mechanical milling (MM), it may be possible to reproduce or even surpass the electrochemical properties of cactus-like MVO.

In this study, we systematically investigated the effect of MM on the crystal structure and electrochemical properties of solid-state synthesized MVO. Detailed structural refinements were performed to clarify how cation disorder and crystallite size evolve with milling. Furthermore, we compared the structural and electrochemical characteristics of MM-derived and ST-derived MVO samples to elucidate the relationship between crystallography and cathode performance.

2 Experimental

2.1 Synthesis

MVO was synthesized mainly by two methods: one was a solid-state synthesis followed by MM to produce fine particles (MM-MVO), and the other was a ST synthesis followed by calcination of the precursor (ST-MVO). The solid-state method for the

former was carried out by using MgO (98.0%, FUJIFILM Wako Pure Chemical) and V_2O_3 (99.0%, FUJIFILM Wako Pure Chemical) as starting materials, grinding and mixing them in a MM using Fritsch P-6 planetary ball mill at 450 rpm for 64 h in ethanol, and then calcining them in a vacuum at 750 °C for 12 h. Pulverization was carried out by MM at 450 rpm using different ZrO_2 ball diameters with ethanol in stages, first for 64 h with a diameter of ϕ 5 mm, then for 16 h with a diameter of ϕ 0.2 mm, and finally for 2 h with a diameter of ϕ 0.1 mm. The ST method for the latter was carried out in ethylene glycol (99.5%, Tokyo Chemical Industry) using NH_4VO_3 (99.0%, FUJIFILM Wako Pure Chemical) and magnesium acetate hydrate (99.9%, FUJIFILM Wako Pure Chemical) as raw materials (180 °C, 24 h) with reference to.²⁴ The obtained precursor was filtered and washed with ethanol, and then calcined at 600 °C in a nitrogen flow for 2 h to obtain ST-MVO.

2.2 Analysis and cathode property

Each product was identified by powder X-ray diffraction (XRD, Cu K α radiation, Rigaku Ultima IV) operated at 40 kV and 50 mA. The diffraction patterns were collected over 2θ ranges of 10–90° with a step size of 0.02° and a scan speed of 2° min^{-1} . Rietveld refinement of the crystal structures was performed using RIETAN-FP.²⁵ Assuming the space group $Fd\bar{3}m$ with a spinel-type framework, possible occupancies of Mg and V atoms were examined not only at the conventional 8a and 16d cation sites but also at the 16c site located between two 8a sites. During the refinement, a constraint was imposed such that the sum of the 8a occupancy and twice the 16c occupancy did not exceed unity. For the samples most finely milled by MM and those synthesized *via* the ST method, additional XRD measurements using Mo K α radiation (Rigaku SmartLab) were carried out to compare their crystal structures in greater detail. The morphology of the obtained products was observed by field-emission scanning electron microscopy (FE-SEM, Hitachi Regulus SU8220), and the crystallite size was estimated using the Halder–Wagner method.²⁶

Electrochemical performance was evaluated following the procedure reported previously,¹⁷ except that a rectangular three-electrode laminated cell (100 mm \times 70 mm, Fig. S1) was employed to suppress side reactions with the stainless-steel cell.²⁷ The cathode was prepared by thoroughly mixing the active material, conductive carbon (Super C65, Timcal), and PTFE binder at a weight ratio of 5 : 5 : 1, pressing the mixture into a ϕ 15 mm pellet, and attaching it to an aluminum-mesh current-collector. Electrical connection was made through an aluminum tab (>99%, Nilaco, 0.05 mm thick, 5 mm \times 50 mm). A magnesium metal foil (99.9%, Rikazai, 0.05 mm thick, 30 mm \times 20 mm) was used as the anode, connected in the same manner. The electrolyte consisted of 0.3 M $[\text{Mg}(\text{G4})][\text{TFSA}]_2/[\text{Pyr}_{13}][\text{TFSA}]$ (approximately 1 mL).¹⁵ A silver reference electrode (99.98%, Nilaco, 0.05 mm thick, 5 mm \times 40 mm) was fixed inside the laminated cell with fusion tape. The cathode and anode were separated by a GA-100 glass fiber filter (30 mm \times 25 mm), while the reference electrode was placed in contact with the separator without touching either working electrode.



The three-electrode cell was placed in a thermostatic chamber at 90 °C. After resting for 12 h, galvanostatic charge–discharge tests were performed using a Hokuto Denko HJ1001SD8c system. The current density was set to 5 mA g^{−1}. Charging was carried out up to 1.0–1.4 V vs. Ag/Ag⁺ (equivalent to 3.6–4.0 V vs. Mg/Mg²⁺), and discharging down to −1.4 or −1.2 V vs. Ag/Ag⁺ (equivalent to 1.2 V or 1.4 V vs. Mg/Mg²⁺), for a total of five cycles. A rest period of 10 min was inserted between each charge and discharge step. The amount of Mg insertion and extraction after charge and discharge of ST-MVO was evaluated by X-ray fluorescence (XRF) analysis after thoroughly washing the electrode with acetonitrile.

2.3 Computational details

First-principles calculations were performed using the projector augmented-wave (PAW) method²⁸ as implemented in the VASP code.²⁹ The r2SCAN exchange–correlation functional³⁰ was employed. We used PAW data sets with radial cutoffs of 1.06, 1.43, and 0.80 Å for Mg, V, and O, respectively, and described Mg-2s and 2p, V-3d and 4s, and O-2s and 2p as valence electrons. To reproduce the experimental open circuit potential (2.3 V vs. Mg/Mg²⁺), we examined the Hubbard *U* correction³¹ on the V-3d orbitals and found the best agreement was obtained with *U*_{eff} = 0 (*i.e.*, without the Hubbard *U* correction). The stable magnetic configuration was determined by considering all ferromagnetic and antiferromagnetic configurations in the primitive cell. Structural relaxation of the pristine was performed using a plane-wave cutoff energy of 520 eV, whereas relaxations of the conventional cell were carried out with a 400 eV cutoff under fixed-cell constraints. Mg migration was evaluated using the Nudged-Elastic band (NEB) method.³²

3 Results and discussion

Fig. 1 shows SEM images of the MVO samples synthesized by the solid-state method and subsequently subjected to stepwise MM. The SEM images reveal that the pristine sample consists of particle sizes within 200–500 nm, while the MM-MVO are pulverized into fine particles smaller than 100 nm.

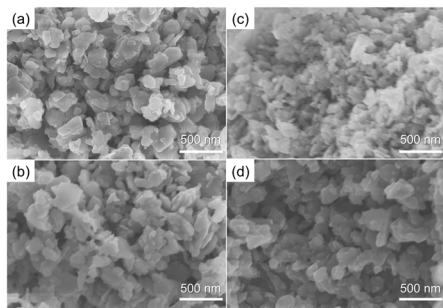


Fig. 1 FE-SEM images of (a) pristine MVO calcined at 750 °C, (a) pristine MVO calcined at 750 °C, (b) 64 h mechanically milled with ϕ 5 mm ZrO₂, (c) +16 h with ϕ 0.2 mm ZrO₂, and (d) +2 h with ϕ 0.1 mm ZrO₂, resulting in 82 h in total.

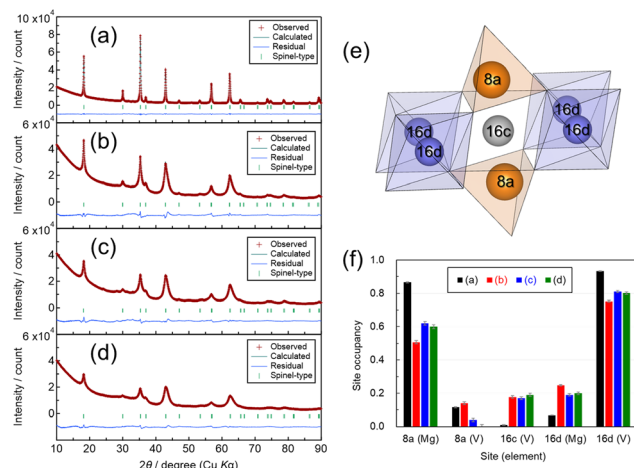


Fig. 2 XRD patterns and Rietveld refinement of (a) pristine MVO calcined at 750 °C, (a) pristine MVO calcined at 750 °C, (b) 64 h mechanically milled with ϕ 5 mm ZrO₂, (c) +16 h with ϕ 0.2 mm ZrO₂, and (d) +2 h with ϕ 0.1 mm ZrO₂, resulting in 82 h in total. Metal arrangement (e) of 8a, 16c and 16d site in spinel-type structure. Refined site occupancies (f) at 8a, 16c and 16d sites derived from Rietveld refinement.

The XRD patterns and their Rietveld refinements are shown in Fig. 2(a–d). All the diffraction patterns can be indexed to a spinel-type structure. The gradual broadening of the diffraction peaks with increasing milling time indicates a reduction in crystallite size accompanied by particle fragmentation. The crystallite sizes estimated by the Halder–Wagner method were 45.6 nm (pristine), 20.8 nm (MM 64 h, ϕ 5 mm), 6.41 nm (MM 64 h + 16 h, ϕ 0.2 mm), and 5.32 nm (MM 64 h + 16 h + 2 h, ϕ 0.1 mm), respectively, confirming the progressive reduction of the crystallites. We note that crystallite sizes obtained from the Halder–Wagner method should be interpreted with caution, particularly when significant peak broadening is present. The method assumes that size and strain broadening can be separated, but defects, strain variations, and instrumental effects also contribute, making the absolute crystallite size uncertain. Therefore, the obtained values should be regarded as qualitative or comparative indicators rather than precise absolute dimensions. On the other hand, variations in the relative peak intensities depending on the milling degree suggest changes in the cation occupancies within the spinel lattice. In the Rietveld refinements, models assuming cation deficiency at the 16d site resulted in poor fitting accuracy; therefore, the total occupancy at the 16d site was fixed to unity. In the spinel structure, the metal sites 8a, 16c, and 16d are in the relationship shown in Fig. 2(e), with the 16c site located between the 8a sites. If a metal occupies 16c, the two adjacent 8a sites cannot be occupied because they are too close to the 16c metal. The occupancies at 8a and 16c are subject to the constraints set out above. The refined occupancies of Mg and V at the 8a, 16d, and 16c sites are summarized in Fig. 2(f). The pristine sample exhibited nearly full Mg occupancy at the 8a site and V occupancy at the 16d site, indicating an ordered normal spinel configuration. In contrast, all MM samples exhibited increased cation disorder, and in the



most heavily milled sample, a significant V occupancy (0.194 ± 0.010) was observed at the 16c site, suggesting severe cation redistribution. While V K-edge XAS and neutron techniques have excellent accuracy for refining the presence of V at the 16c site, laboratory XRD should also provide sufficient sensitivity, as the X-ray scattering coefficients of Mg^{2+} and V^{3+} are significantly different, reflecting the two-fold difference in electron numbers. This contrast allows for significant refinement of the cation distribution using the Rietveld refinement, with all refined metal site occupancies having estimated standard deviations (ESDs) ranging from 0.007 to 0.011. Considering the solid-state diffusion of Mg^{2+} during charge–discharge, smaller particle sizes are generally favourable due to the shorter diffusion paths. However, since the 16c sites act as migration channels for Mg^{2+} , their partial occupation by V could block the conduction pathways. Therefore, excessive milling does not necessarily improve the electrochemical performance of the cathode.

The electrochemical properties of each sample are shown in Fig. 3. Although direct quantitative comparison is limited due to differing experimental conditions, the pristine sample (Fig. 3(a)) maintained a discharge capacity of approximately 70 mAh g^{-1} over five cycles. In contrast, the MM samples exhibited unstable discharge capacities that fluctuated between cycles, implying significant side reactions. All samples except that in Fig. 3(c) displayed pronounced side reactions during charging (Fig. S2). The GITT curve for the MM sample (82 h total) revealed that the charging potential did not reach $3.0 \text{ V vs. Mg/Mg}^{2+}$ after 60 mAh g^{-1} due to side reactions (Fig. S3a). MgV_2O_4 nanocrystals have been reported to decompose electrolytes at high temperatures.³³ These results suggest that moderate particle sizes in the range of 20–100 nm are optimal. Nonetheless, the observed capacities ($<90 \text{ mAh g}^{-1}$) were much lower than the theoretical capacity of 282 mAh g^{-1} , and the polarization was considerably large. Thus, the electrochemical performance did

not reach the level previously reported for ST synthesized samples ($\sim 120 \text{ mAh g}^{-1}$ even at high current density of 100 mA g^{-1}).²⁴ For comparison, the GITT curve for ST-MVO (Fig. S3b) shows a smooth increase in potential during charging, corroborating the suppression of side reactions. Furthermore, the overpotential during both charge and discharge is reduced, supporting enhanced Mg^{2+} ionic transport. Because excessive milling was found to deteriorate performance—likely due to V atoms blocking the 16c diffusion paths—the most heavily milled sample was further investigated using VASP calculations.

To support our experimental findings, we performed first-principles calculations. We created a single Mg vacancy in the conventional cell of an ordered normal spinel containing 8 Mg (8a site), 16 V (16d site), and 32 O atoms, and calculated the Mg migration barrier using the NEB method. Fig. 4(a and b) show that Mg migrates through the 16c site during diffusion with the activation barrier of 0.62 eV. Thus, occupation of the 16c sites by V atoms, as observed in MM samples, is expected to hinder the Mg migration. Furthermore, to reproduce the crystal structure refined from the MM-MVO, we randomly moved four V atoms from 16d sites to 16c sites (deep blue spheres in Fig. 4(c)) and moved four Mg atoms to the empty 16d sites (yellow spheres in Fig. 4(c)) from the ordered spinel structures. After structure optimization, all Mg atoms originally located at the 16d sites remained at the 16d sites; in contrast, two of the V atoms at the 16c sites moved to the 8a sites, while the other two stayed at 16c sites in Fig. 4(d). These results demonstrate that V can occupy both the 16d and 16c sites when they are excited to these positions, in good agreement with our experimental observations. We also relaxed the atomic positions of the disordered spinel, *i.e.*, $\text{Mg}_{0.5}\text{V}_{0.5}$ at the 8a site and $\text{Mg}_{0.25}\text{V}_{0.75}$ at the 16d sites, and confirmed that all Mg and V atoms remained at their local positions. We also investigated the V migration barrier from the 16d to the 16c sites. For this calculation, two Mg atoms along the

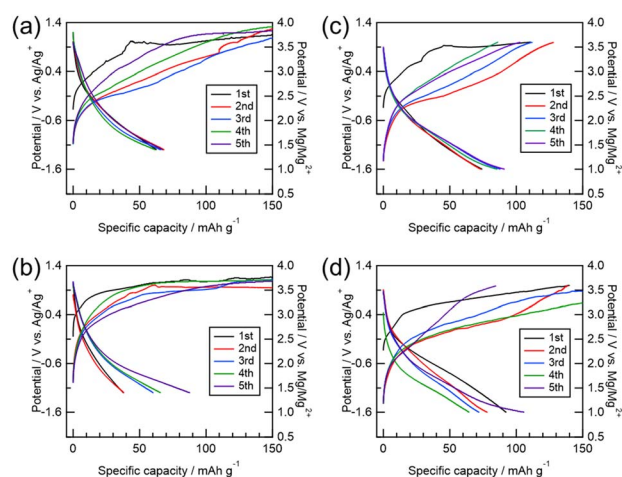


Fig. 3 Charge–discharge curves were measured using a three-electrode cell with a quasi-reference electrode. The left vertical axis indicates the potential versus the quasi-reference, while the right axis shows the corresponding values converted to the Mg/Mg^{2+} scale: (a) pristine MVO calcined at 750°C , (b) 64 h mechanically milled with ϕ 5 mm ZrO_2 , (c) +16 h with ϕ 0.2 mm ZrO_2 , and (d) +2 h with ϕ 0.1 mm ZrO_2 , resulting in 82 h in total.

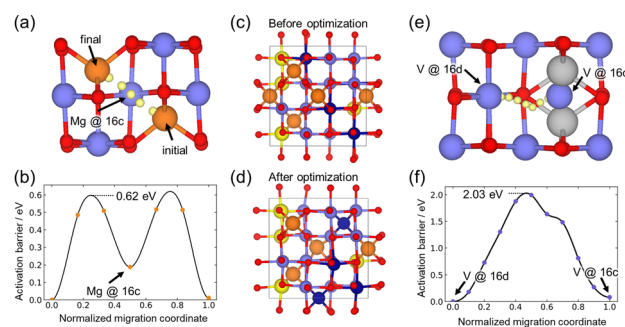


Fig. 4 Mg migration and disordered structures of MgV_2O_4 from DFT calculations. (a) Mg migration pathway from the initial to the final position. Red, purple, and orange spheres are O, V, and Mg, respectively. Small yellow spheres are the intermediate positions of the migrating Mg atom. (b) Energy profile along the Mg migration path. (c and d) Disordered MgV_2O_4 structures before and after structure optimization. Yellow and deep blue spheres are Mg and V which are intentionally located at the 16d and 8a sites (see the documents for details), respectively. (e) V migration pathway from the 16d to 16c sites. The gray spheres are removed Mg sites. (f) Energy profile along the V migration path shown in (e).



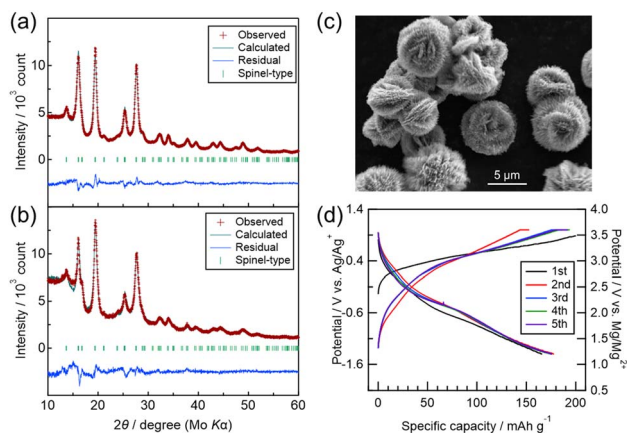


Fig. 5 Rietveld refinements for XRD patterns of MVO (a) synthesized at 600 °C *via* solvothermal method and (b) calcined at 750 °C and subsequently ball-milled for a total of 82 h. (c) SEM image of MVO synthesized at 600 °C *via* solvothermal method. (d) Charge and discharge cycle-curves of MVO synthesized at 600 °C *via* solvothermal method.

migration pathway were removed as shown in Fig. 4(e) because their strong Mg–V Coulomb interactions destabilized the NEB calculations. Still, the resultant migration barrier was approximately 2.0 eV, which is considerably larger than the Mg migration barrier. These results indicate that thermal activation alone is insufficient to move V to 16c sites, and mechanical milling is expected to provide enough energy to facilitate the V migrations. Consequently, these results demonstrate a clear limitation in improving the electrochemical properties of MgV_2O_4 through mechanical milling alone.

To overcome this limitation, a sample synthesized *via* a ST route was evaluated. As shown in the $\text{Mo K}\alpha$ XRD data (Fig. 5(a)), the ST-derived and MM-derived (Fig. 5(b)) samples exhibited similar diffraction patterns, indicating that the ST method can produce fine crystallites without mechanical milling. SEM observations in Fig. 5(c) revealed cactus-like particles with diameters of approximately 5 μm , which can be regarded as secondary particles composed of radially assembled needle-like crystallites. Although the diameter of each needle-like crystallite is too small to be measured by SEM, XRD analysis using the Halder–Wagner method revealed a crystallite size of 5.38 nm, comparable to that of MM-MVO (5.32 nm). This indicates that the short-axis direction of each needle-like crystal provides a sufficiently short Mg^{2+} diffusion length, while the long-axis direction remains relatively long, which may help suppress

side reactions. Considering that the spinel structure enables three-dimensional diffusion, the combination of shortened two dimensions and elongated one dimension can still offer significant benefits. Moreover, Rietveld refinement of the ST-MVO revealed the following site occupancies: $(\text{Mg}_{0.692(8)}\text{V}_{0.070(8)})_{8a}(\text{V}_{0.119(7)})_{16c}(\text{Mg}_{0.154(6)}\text{V}_{0.846(6)})_{16d}$. Compared with MM-MVO (Fig. 2(f)), the ST-MVO exhibits a lower V occupancy (0.119 ± 0.007) at the 16c site and higher Mg and V occupancies at the 8a and 16d sites, respectively, indicating a more ordered spinel structure.

The electrochemical performance of this sample, shown in Fig. 5(d), demonstrated a reversible charge–discharge capacity of $175 \pm 2 \text{ mAh g}^{-1}$. Compared with the MM samples, the polarization was smaller, and the average discharge potential reached $1.95 \pm 0.04 \text{ V vs. Mg/Mg}^{2+}$. These results highlight the advantage of the cactus-like microstructure, which maintains low V occupancy at the 16c site while effectively utilizing fine crystallites for Mg^{2+} insertion and extraction. In previous studies²⁴ employing less oxidative-stable grignard-based electrolytes, charging was limited to 2.0 V vs. Mg/Mg^{2+} , resulting in capacities of $\sim 100 \text{ mAh g}^{-1}$. In contrast, the present electrolyte allowed charging up to 3.6 V vs. Mg/Mg^{2+} , enabling greater Mg extraction and thus higher capacity. On the other hand, under the high-temperature cycling at 90 °C, the degradation becomes evident due to the reductive decomposition of the TFSA anions on anode surface. Moreover, the coordinated G4 molecules in the electrolyte would undergo thermal decomposition *via* being contact with MgV_2O_4 at elevated temperature.³³ The cross-over from cathode-electrolyte interface to Mg anode can also induce impedance growth and consequent cell failure, especially under high temperature operation.³⁴ To gain deeper understanding of the events taking place at both electrode–electrolyte interface, further investigations beyond the five cycles are necessary. Quantitative XRF analysis of the electrodes after washing with acetonitrile showed Mg/V ratios of 0.63 (charged) and 1.29 (discharged), confirming the reversible insertion/extraction of approximately 0.66 Mg^{2+} per formula unit. This corresponds to a calculated capacity of 186 mAh g^{-1} , quite consistent with the measured capacity. These findings suggest that the ST-MVO exhibits both deintercalation-type behavior similar to that of LiMn_2O_4 spinel and insertion-type behavior resembling $\text{Li}_4\text{Mn}_5\text{O}_{12}$ spinel,³⁵ resulting in enhanced capacity. Further improvement may be achievable by developing electrolytes or solid electrolytes with higher oxidative stability, which would enable deeper charging and

Table 1 Comparison of cathode properties among typical MgTM_2O_4 spinel series

	Electrolyte	Temp./°C	Potential/V	Capacity/mAh g^{-1}	Starting reaction	Reversibility
MgV_2O_4 (this study)	$[\text{Mg}(\text{G4})][\text{TFSA}]_2/[\text{PyT}_{13}][\text{TFSA}]$	90	2	175	Deintercalation	106% (5th/1st) 99% (5th/2nd)
MgV_2O_4 (ref. 24)	$(\text{PhMgCl})_2\text{-AlCl}_3/\text{THF}$	RT	≈ 0.7	132	Deintercalation	85% (300th/1st)
MgCo_2O_4 (ref. 10)	$(\text{Mg}10/\text{Cs}90)\text{-TFSA}$	150	≈ 2.5	170	Insertion	71% (2nd/1st)
$\text{MgFe}_{1.6}\text{Mn}_{0.4}\text{O}_4$ (ref. 18)	$[\text{Mg}(\text{G4})][\text{TFSA}]_2/[\text{PyT}_{13}][\text{TFSA}]$	100	≈ 1.4	≈ 200	Insertion	45% (10th/1st)
MgMn_2O_4 (ref. 19)	$[\text{Mg}(\text{G4})][\text{TFSA}]_2/[\text{PyT}_{13}][\text{TFSA}]$	100	2	214	Insertion	46% (5th/1st)
MgCrMnO_4 (ref. 20)	$\text{Mg}[\text{TPFA}]_2/\text{G3}$	60	≈ 1.8	75	Deintercalation	59% (2nd/1st)



approach the theoretical capacity. Previous spinel-type MgTM_2O_4 (TM = Co,^{9,10} Mn,^{19,22} Fe,¹⁸ Cr,²⁰ etc.) cathodes have generally shown insertion-type behavior upon discharge, and their capacity fade has been attributed to irreversible transition to a rock-salt $\text{Mg}_2\text{TM}_2\text{O}_4$ phase. The cathode properties of typical MgTM_2O_4 spinel series are summarized in Table 1. The ST-MVO developed in this study exhibits a high potential and capacity, suggesting its superior reversibility. This behavior is attributed to a reaction pathway initiated by demagnesiumation, combined with the favorable Mg^{2+} conduction inherent to the material. Further optimization of the synthesis conditions may allow additional modification of the ball cactus-like morphology and crystallographic order in cation sites. Combined with the use of high oxidative-stability electrolytes suitable for long-term cycling, ST-MVO has the potential to evolve into a highly practical cathode material in MRBs.

4 Conclusions

It was generally believed that fine particles produced by MM exhibited high cathode properties, but it was found that this was not applicable to MVO because the MM caused V to move into the Mg^{2+} conduction site, 16c, hindering Mg deintercalation and intercalation. However, in the field of MRB spinel cathodes, which have previously operated in an insertion-type manner, the fact that ST-MVO is an important cathode material capable of starting charging is a major step forward. By using the ST method, MVO can be synthesized at low temperature of 600 °C, and it is possible to obtain MVO that is closer to the order arrangement while still having nanocrystallites. When charged to a potential equivalent to 3.6 V vs. Mg/Mg^{2+} , the cell delivered 175 mAh g⁻¹, 62% of the theoretical capacity, representing an improvement of more than 40% over the capacity reported in the previous study. With further optimization of the solvothermal synthesis conditions, MgV_2O_4 with improved morphology and structural ordering may achieve capacities closer to the theoretical value of 282 mAh g⁻¹. At the same time, the development of electrolytes with higher oxidative and thermal stability, particularly beyond the known degradation limits of TFSA/G4 at 90 °C, will be essential for fully realizing the practical potential of MVO-based MRBs.

Author contributions

N. Ishida: conceptualization, data curation, formal analysis, investigation, project administration, supervision, writing – original draft, writing – review & editing. K. Kubota: investigation, methodology, resources, validation. T. Kojima: investigation, methodology, resources. T. Mandai: investigation, resources, writing – review & editing. S. Kiyohara and Y. Kumagai: conceptualization, formal analysis, investigation, visualization, writing – original draft. T. Ichitsubo: funding acquisition, project administration, supervision.

Conflicts of interest

There are no conflicts to declare.

Data availability

The data supporting this article have been included as part of the supplementary information (SI). Supplementary information: laminated three-electrode cell, charge/discharge curves, GITT curves, and fitting of PDF. See DOI: <https://doi.org/10.1039/d5ta09602b>.

Acknowledgements

This work was supported by JST GteX Program Japan Grant Number JPMJGX23S1.

References

- 1 X. Yu and A. Manthiram, Sustainable Battery Materials for Next-Generation Electrical Energy Storage, *Adv. Energy Sustainability Res.*, 2021, 2, 2000102, DOI: [10.1002/aesr.202000102](https://doi.org/10.1002/aesr.202000102).
- 2 D. Aurbach, Z. Lu, A. Schechter, Y. Gofer, H. Gizbar, R. Turgeman, Y. Cohen, M. Moshkovich and E. Levi, Prototype systems for rechargeable magnesium batteries, *Nature*, 2000, 407, 724–727, DOI: [10.1038/35037553](https://doi.org/10.1038/35037553).
- 3 R. D. Shanon, Revised effective ionic radii and systematic studies of interatomic distances in halides and chalcogenides, *Acta Crystallogr.*, 1976, A32, 751–767, DOI: [10.1107/S0567739476001551](https://doi.org/10.1107/S0567739476001551).
- 4 Z. Li, J. Häcker, M. Fichtner and Z. Zhao-Karger, Cathode Materials and Chemistries for Magnesium Batteries: Challenges and Opportunities, *Adv. Energy Mater.*, 2023, 13, 2300682, DOI: [10.1002/aenm.202300682](https://doi.org/10.1002/aenm.202300682).
- 5 X. Ge, F. Song, A. Du, Y. Zhang, B. Xie, L. Huang, J. Zhao, S. Dong, X. Zhou and G. Cui, Robust Self-Standing Single-Ion Polymer Electrolytes Enabling High-Safety Magnesium Batteries at Elevated Temperature, *Adv. Energy Mater.*, 2022, 12, 2201464, <https://advanced.onlinelibrary.wiley.com/doi/full/10.1002/aenm.202201464>.
- 6 O. Chusid, Y. Gofer, H. Gizbar, Y. Vestfrid, E. Levi, D. Aurbach and I. Riech, Solid-State Rechargeable Magnesium Batteries, *Adv. Mater.*, 2003, 15, 627–630, DOI: [10.1002/adma.200304415](https://doi.org/10.1002/adma.200304415).
- 7 M. Matsui, Study on electrochemically deposited Mg metal, *J. Power Sources*, 2011, 196, 7048–7055, DOI: [10.1016/j.jpowsour.2010.11.141](https://doi.org/10.1016/j.jpowsour.2010.11.141).
- 8 D. Aurbach, I. Weissman, Y. Gofer and E. Levi, Nonaqueous magnesium electrochemistry and its application in secondary batteries, *Chem. Rec.*, 2003, 3, 61–73, DOI: [10.1002/tcr.10051](https://doi.org/10.1002/tcr.10051).
- 9 T. Ichitsubo, T. Adachi, S. Yagi and T. Doi, Potential positive electrodes for high-voltage magnesium-ion batteries, *J. Mater. Chem.*, 2011, 21, 11764–11772, DOI: [10.1039/C1JM11793A](https://doi.org/10.1039/C1JM11793A).
- 10 S. Okamoto, T. Ichitsubo, T. Kawaguchi, Y. Kumagai, F. Oba, S. Yagi, K. Shimokawa, N. Goto, T. Doi and E. Matsubara, Intercalation and Push-Out Process with Spinel-to-Rocksalt Transition on Mg Insertion into Spinel Oxides in



- Magnesium Batteries, *Adv. Sci.*, 2015, **2**, 1500072, DOI: [10.1002/advs.201500072](https://doi.org/10.1002/advs.201500072).
- 11 Y. Orikasa, T. Masese, Y. Koyama, T. Mori, M. Hattori, K. Yamamoto, T. Okado, Z.-D. Huang, T. Minato, C. Tassel, J. Kim, Y. Kobayashi, T. Abe, H. Kageyama and Y. Uchimoto, High energy density rechargeable magnesium battery using earth-abundant and non-toxic elements, *Sci. Rep.*, 2014, **4**, 5622, DOI: [10.1038/srep05622](https://doi.org/10.1038/srep05622).
 - 12 N. Ishida, R. Nishigami, N. Kitamura and Y. Idemoto, Crystal Structure Analysis and Electrochemical Properties of Chemically Delithiated $\text{Li}_{0.13}\text{Mn}_{0.54}\text{Ni}_{0.13}\text{Co}_{0.13}\text{O}_{2-\delta}$ as Cathode Material for Rechargeable Mg Batteries, *Chem. Lett.*, 2017, **46**, 1508, DOI: [10.1246/cl.170615](https://doi.org/10.1246/cl.170615).
 - 13 N. Ishida, R. Nishigami, M. Matsui, T. Mandai, K. Kanamura, N. Kitamura and Y. Idemoto, Revisiting Delithiated $\text{Li}_{1.2}\text{Mn}_{0.54}\text{Ni}_{0.13}\text{Co}_{0.13}\text{O}_2$: Structural Analysis and Cathode Properties in Magnesium Rechargeable Battery Applications, *Electrochemistry*, 2021, **89**, 329–333, DOI: [10.5796/electrochemistry.21-00038](https://doi.org/10.5796/electrochemistry.21-00038).
 - 14 M. Kotobuki, B. Yan and L. Lu, Recent progress on cathode materials for rechargeable magnesium batteries, *Energy Storage Mater.*, 2023, **54**, 227–253, DOI: [10.1016/j.ensm.2022.10.034](https://doi.org/10.1016/j.ensm.2022.10.034).
 - 15 T. Mandai, K. Tatesaka, K. Soh, H. Masu, A. Choudhary, Y. Tateyama, R. Ise, H. Imai, T. Takeguchi and K. Kanamura, Modifications in coordination structure of $\text{Mg}[\text{TFSA}]_2$ -based supporting salts for high-voltage magnesium rechargeable batteries, *Phys. Chem. Chem. Phys.*, 2019, **21**, 12100–12111, DOI: [10.1039/C9CP01400D](https://doi.org/10.1039/C9CP01400D).
 - 16 N. Ishida, N. Yamazaki, T. Mandai, N. Kitamura and Y. Idemoto, Crystal Structures and Cathode Properties of Chemically and Electrochemically Delithiated $\text{Li}_x\text{Ni}_{0.5}\text{Mn}_{0.5}\text{O}_2$ with Applications to Mg Rechargeable Batteries, *J. Electrochem. Soc.*, 2020, **167**, 100547, DOI: [10.1149/1945-7111/ab9b9b](https://doi.org/10.1149/1945-7111/ab9b9b).
 - 17 N. Ishida, Y. Nakamura, T. Mandai, N. Kitamura and Y. Idemoto, Synthesis, cathode property and crystal, electronic and local structures of $\text{Mg}_2\text{Mo}_3\text{O}_8$ as Mg rechargeable battery cathode material, *Solid State Ionics*, 2020, **354**, 115413, DOI: [10.1016/j.ssi.2020.115413](https://doi.org/10.1016/j.ssi.2020.115413).
 - 18 J. Han, S. Yagi and T. Ichitsubo, Suppressive effect of Fe cations in $\text{Mg}(\text{Mn}_{1-x}\text{Fe}_x)_2\text{O}_4$ positive electrodes on oxidative electrolyte decomposition for Mg rechargeable batteries, *J. Power Sources*, 2019, **435**, 226822, DOI: [10.1016/j.jpowsour.2019.226822](https://doi.org/10.1016/j.jpowsour.2019.226822).
 - 19 K. Ishii, S. Doi, R. Ise, T. Mandai, Y. Oaki, S. Yagi and H. Imai, Structured spinel oxide positive electrodes of magnesium rechargeable batteries: High rate performance and high cyclability by interconnected bimodal pores and vanadium oxide coating, *J. Alloys Compd.*, 2020, **816**, 152556, DOI: [10.1016/j.jallcom.2019.152556](https://doi.org/10.1016/j.jallcom.2019.152556).
 - 20 B. J. Kwon, L. Yin, H. Park, P. Parajuli, K. Kumar, S. Kim, M. Yang, M. Murphy, P. Zapol, C. Liao, T. T. Fister, R. F. Klie, J. Cabana, J. T. Vaughey, S. H. Lapidus and B. Key, High Voltage Mg-Ion Battery Cathode via a Solid Solution Cr–Mn Spinel Oxide, *Chem. Mater.*, 2020, **32**, 6577–6587, DOI: [10.1021/acs.chemmater.0c01988](https://doi.org/10.1021/acs.chemmater.0c01988).
 - 21 Y. Idemoto, M. Ichiyama, N. Ishida and N. Kitamura, Structural and electronic properties of spinel type $\text{Mg}_{1+y}\text{Co}_{2-x-y}\text{Mn}_x\text{O}_4$ for cathode applications in magnesium rechargeable batteries, *J. Power Sources*, 2021, **482**, 228920, DOI: [10.1016/j.jpowsour.2020.228920](https://doi.org/10.1016/j.jpowsour.2020.228920).
 - 22 H. Kobayashi, Y. Fukumi, H. Watanabe, R. Iimura, N. Nishimura, T. Mandai, Y. Tominaga, M. Nakayama, T. Ichitsubo, I. Honma and H. Imai, Ultraporos, Ultrasmall MgMn_2O_4 Spinel Cathode for a Room-Temperature Magnesium Rechargeable Battery, *ACS Nano*, 2023, **17**, 3135–3142, DOI: [10.1021/acsnano.2c12392](https://doi.org/10.1021/acsnano.2c12392).
 - 23 Y. Idemoto, N. Kawakami, N. Ishida and N. Kitamura, Synthesis, electrochemical properties, and changes in crystal and electronic structures during charge/discharge process of spinel-type cathode materials $\text{Mg}_4\text{V}_{5-x}\text{Ni}_x\text{O}_{12}$ ($x = 0, 0.3, 0.6, 1.0$) for magnesium secondary batteries, *J. Power Sources*, 2020, **455**, 227962, DOI: [10.1016/j.jpowsour.2020.227962](https://doi.org/10.1016/j.jpowsour.2020.227962).
 - 24 Q. Ding, T. Han, T. Zhou, X. Lin and J. Liu, A Temperature-Tolerant Magnesium-Ion Battery Using Ball Cactus-like MgV_2O_4 as High-Performance Cathode, *Chem.–Eur. J.*, 2024, **30**, e202302978, DOI: [10.1002/chem.202302978](https://doi.org/10.1002/chem.202302978).
 - 25 F. Izumi and K. Momma, Three-Dimensional Visualization in Powder Diffraction, *Solid State Phenom.*, 2007, **130**, 15–20, DOI: [10.4028/www.scientific.net/SSP.130.15](https://doi.org/10.4028/www.scientific.net/SSP.130.15).
 - 26 N. C. Halder and C. N. J. Wagner, Separation of particle size and lattice strain in integral breadth measurements, *Acta Crystallogr.*, 1966, **20**, 312, DOI: [10.1107/S0365110X66000628](https://doi.org/10.1107/S0365110X66000628).
 - 27 R. Zhu, T. Yabu, C. Yang, H. Yang, A. Nasu, T. Mandai, M. Matsui and H. Kobayashi, Decoding Cathode-Electrolyte Interface Issues in Conventional Ethers Electrolytes-Based Magnesium Rechargeable Batteries, *Adv. Energy Mater.*, 2025, **15**, 2502050, DOI: [10.1002/aenm.202502050](https://doi.org/10.1002/aenm.202502050).
 - 28 P. E. Blöchl, Projector Augmented-wave Method, *Phys. Rev. B:Condens. Matter Mater. Phys.*, 1994, **50**, 17953–17979, DOI: [10.1103/PhysRevB.50.17953](https://doi.org/10.1103/PhysRevB.50.17953).
 - 29 G. Kresse and J. Hafner, Ab Initio Molecular Dynamics for Liquid Metals, *Phys. Rev. B:Condens. Matter Mater. Phys.*, 1993, **47**, 558–561, DOI: [10.1103/PhysRevB.47.558](https://doi.org/10.1103/PhysRevB.47.558).
 - 30 J. W. Furness, A. D. Kaplan, J. Ning, J. P. Perdew and J. Sun, Accurate and Numerically Efficient r2SCAN Meta-Generalized Gradient Approximation, *J. Phys. Chem. Lett.*, 2020, **11**, 8208–8215, DOI: [10.1021/acs.jpclett.0c02405](https://doi.org/10.1021/acs.jpclett.0c02405).
 - 31 S. L. Dudarev, G. A. Botton, S. Y. Savrasov, C. J. Humphreys and A. P. Sutton, Electron-energy-loss spectra and the structural stability of nickel oxide: An LSDA+U study, *Phys. Rev. B:Condens. Matter Mater. Phys.*, 1998, **57**, 1505, DOI: [10.1103/PhysRevB.57.1505](https://doi.org/10.1103/PhysRevB.57.1505).
 - 32 H. J. Ånsson, G. Mills and K. W. Jacobsen Nudged elastic band method for finding minimum energy paths of transitions, *Chapter 16 in Classical and Quantum Dynamics in Condensed Phase Simulations*, World Scientific, Singapore, 1998, p. 385, DOI: [10.1142/3816](https://doi.org/10.1142/3816).
 - 33 J. Z. Hu, W. Hu, H. Jeong, G. Alexander, N. D. Thien, V. Prabhakaran, K. S. Han, Y. Chen, J. Cabana, J. G. Connell, L. Cheng, V. Murugesan, K. R. Zavadil and



- K. T. Mueller, Thermal decomposition pathway of bulk electrolytes on vanadium oxide nanocrystals, *Energy Storage Mater.*, 2025, 79, 104315, DOI: [10.1016/j.ensm.2025.104315](https://doi.org/10.1016/j.ensm.2025.104315).
- 34 D. Setiawan, O. Falyouna and T. Mandai, Beyond Half-Cell Success: Cathode-Electrolyte Reactivity Driving Magnesium Battery Full-Cell Degradation at Elevated Temperature, *Adv. Sci.*, 2025, 12, e11416, DOI: [10.1002/advs.202511416](https://doi.org/10.1002/advs.202511416).
- 35 M. M. Thackeray, Manganese oxides for lithium batteries, *Prog. Solid State Chem.*, 1997, 25, 1–71, DOI: [10.1016/S0079-6786\(97\)81003-5](https://doi.org/10.1016/S0079-6786(97)81003-5).

